Journal of Power Sources 652 (2025) 237322

Contents lists available at ScienceDirect

Journal of Power Sources

journal homepage: www.elsevier.com/locate/jpowsour

# Increasing the cycling stability of LLZO-based solid-state batteries with $Li_3BO_3$ as catholyte

Walter Sebastian Scheld [a,*], Yannic Collette [a,b], Kaouther Touidjine [a,b], Christoph Roitzheim [a], Yoo Jung Sohn [a], Dina Fattakhova-Rohlfing [a,b,c,**]

[a] Forschungszentrum Jülich GmbH, Institute of Energy and Climate Research, Materials Synthesis and Processing IMD-2, 52425, Jülich, Germany
[b] University of Duisburg-Essen, Faculty of Engineering and Center for Nanointegration Duisburg-Essen CENIDE, Lotharstraße 1, 47057, Duisburg, Germany
[c] Jülich Aachen Research Alliance JARA-ENERGY, 52425, Jülich, Germany

## HIGHLIGHTS

- $Li_3BO_3$ (LBO) was used as catholyte material in the composite cathode.
- Less capacity fading compared to $Li_7La_3Zr_2O_{12}$ (LLZO) based composite cathodes.
- The composite cathode was investigated before and after cycling.
- Lower ionic conductive materials than LLZO can still rival it in cycling stability.

## ARTICLE INFO

*Keywords:*
Solid-state battery
LLZO
$Li_7La_3Zr_2O_{12}$
$Li_3BO_3$
NMC
Electrochemical energy storage

## ABSTRACT

Solid-state batteries (SSB) are a promising technology for the future battery market to get cells with high safety and high energy density. Oxide-based SSBs with garnet $Li_7La_3Zr_2O_{12}$ solid-state electrolytes have thereby in particular advantageous properties, like high temperature resistance, non-toxicity, and a high stability towards Li metal anodes. However, those cells have one major challenge that must be overcome for a future commercial implementation, which is the electrochemical instability with the common cathode active materials during electrochemical operation, which results in capacity fading. In this work it was shown that the capacity fading can be reduced by exchanging the solid-state electrolyte in the composite cathode by $Li_3BO_3$. The resulting cells showed a much lower electrochemical performance degradation during cycling compared to similar cells with $Li_7La_3Zr_2O_{12}$ as catholyte. The phases, element distribution, and cell performance was analyzed, and furthermore postmortem analysis was performed to get a full insight into the system. However, despite the improvement of the cycling stability, electrochemically induced cracking of $Li_3BO_3$ in the cathode was observed. This work shows that even materials with lower ionic conductivity are able to provide better cycling behavior compared to composite cathodes based on $Li_7La_3Zr_2O_{12}$.

## 1. Introduction

Lithium solid-state batteries (SSBs) could be the next technology generation of electrochemical energy storage systems by replacing the current Li-ion technology [1]. The liquid electrolyte is thereby exchanged by a solid electrolyte, reaching new levels of safety, thermal stability and energy densities if a Li-metal anode is used [1–4]. The oxide ceramic materials like $Li_7La_3Zr_2O_{12}$ (LLZO) are particularly attractive because they offer a high reduction stability that allows the implementation of Li metal anodes, and simultaneously offer a high ionic conductivity of around $10^{-3}$ S $cm^{-1}$ at room temperature, and are non-flammable [5,6].

The LLZO material is commonly used in two different components of the cell. First, it is used as separator where it additionally serves as solid

* Corresponding author.
** Corresponding author. Forschungszentrum Jülich GmbH, Institute of Energy and Climate Research, Materials Synthesis and Processing IMD-2, 52425, Jülich, Germany.
*E-mail addresses:* s.scheld@fz-juelich.de (W.S. Scheld), y.collette@fz-juelich.de (Y. Collette), k.touidjine@extern.fz-juelich.de (K. Touidjine), c.roitzheim@fz-juelich.de (C. Roitzheim), y.sohn@fz-juelich.de (Y.J. Sohn), d.fattakhova-rohlfing@fz-juelich.de (D. Fattakhova-Rohlfing).

https://doi.org/10.1016/j.jpowsour.2025.237322
Received 15 October 2024; Received in revised form 2 May 2025; Accepted 7 May 2025
Available online 13 June 2025

electrolyte, and secondly it is located in the cathode, where ion-conduction is provided via a LLZO percolation network in the electrode, the so-called composite cathode [4,7]. Those electrodes are fabricated in a high-temperature (>1000 °C) sintering process, where the ion-conducting interfaces between the individual LLZO and cathode active material (CAM) grains are generated [4,8–11]. Due to limited thermal stability between common CAMs and LLZO, the material combination must be specifically selected and sintering temperature and -time must be as low and short as possible to prevent chemical decomposition and secondary phase formations [10–20]. However, even when the processing parameters are adjusted to the materials, a certain interaction is still possible under high-temperature sintering conditions due to a cobalt-ion diffusion that can take place from the CAM into the LLZO grains, changing slightly the electrochemical properties of the electrolyte and leading to secondary phase formation [21,22]. Additionally, most of the CAMs show no stable electrochemical cycling when in contact with LLZO [23,24]. Those cells show a strong increase in cell resistances during cycling, while the specific capacity of the CAM fades from the first cycle to the subsequent cycles [9–11,23,24]. Considering both, the high-temperature LLZO-CAM interaction and the unstable LLZO|CAM interface during electrochemical cycling, cell designs with direct contact of LLZO and CAM, as shown in Fig. 1a are not practical.

A more logical cell design would be the substitution of LLZO in the composite cathode by another catholyte (electrolyte which is only located in the composite cathode), while LLZO is still used as a separator to enable the use of metallic Li anodes, like shown in Fig. 1b. The catholyte should be stable with LLZO and the CAM during the thermal fabrication process and during electrochemical cycling. Further, to reduce possible side reactions and lowering the energy consumption of the composite cathode fabrication it would be beneficial when the catholyte has a low melting/sintering temperature.

A material, which combines a low melting point at ~700 °C and a moderate room-temperature ionic conductivity of around $2 \times 10^{-6}$ S $cm^{-1}$ is $Li_3BO_3$ (LBO) [25]. The thermal and electrochemical stability of LBO with LLZO and different CAMs were already shown in many reports

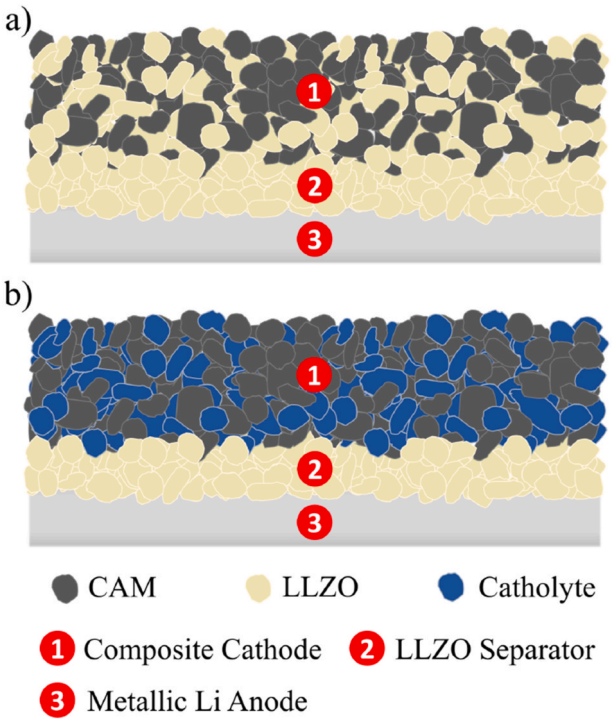


**Fig. 1.** Two different possible SSB designs: a) with LLZO in the separator and composite cathode, b) LLZO only in the separator and another electrolyte (catholyte) in the composite cathode.

[25–33], where LBO is often used as a coating, sintering additive, or consolidation tool. Ohta et al. and Park et al. tested the cell design of Fig. 1b where they used LBO as catholyte with $LiCoO_2$ CAM and LLZO separator [25,30]. They show very promising results with a reduced capacity fading of the LBO cell design compared to common CAM-LLZO cells. However, the phase stability and microstructure were not investigated, which is an essential key for the long-term stability of the material.

Therefore, in this work a SSB with a composite cathode consisting of $LiNi_{0.333}Mn_{0.333}Co_{0.333}O_2$ (NMC111) and LBO and a LLZO separator were fabricated and in detail analyzed. Chemical phases, element diffusion, and the microstructure were investigated after high-temperature processing, and after electrochemical cycling to get knowledge about the suitability of LBO as catholyte. In addition, the cell performance was tested with galvanostatic cycling and impedance spectroscopy. This work shows that even catholyte materials with lower ionic conductivity are able to provide better cycling behavior compared to composite cathodes with LLZO catholyte.

## 2. Experimental

### 2.1. LLZO separator fabrication

Ta- and Al-substituted LLZO ($Li_{6.45}Al_{0.05}La_3Zr_{1.6}Ta_{0.4}O_{12}$) powder was synthesized for the separator fabrication by a three-step solid-state reaction [34–37]. $LiOH{\bullet}H_2O$ (Applichem, 99.00 %), $La_2O_3$ (Merck, 99.90 %, predried at 900 °C for 10 h), $ZrO_2$ (Treibacher, 99.70 %), $Ta_2O_5$ (Treibacher, 99.99 %), and $Al_2O_3$ (Inframat, 99.82 %), were dry-milled and stoichiometrically mixed with a Li excess of 20 mol% $LiOH{\bullet}H_2O$. The resulting powder was pressed into pellets (uniaxial, Ø 45 mm, 19 MPa) and calcined in an $Al_2O_3$ crucible at 850 °C and 1000 °C for 20 h each. In between the calcination steps, the powder was ground and pressed. Finally, powder pellets were pressed (uniaxial, Ø 13 mm, 113 MPa) and sintered in an $Al_2O_3$ crucible with a MgO plate and a LLZO powder sheet at 1175 °C with a dwell time of 10 h. Those pellets were cut into separators of ~400 μm thickness for subsequent SSB fabrication [34–37].

### 2.2. Composite cathode fabrication

First, $Li_3BO_3$ was synthesized by mixing $H_3BO_3$ (Sigma Aldrich, >99.5 %) with $LiOH{\bullet}H_2O$ (Applichem, 99.00 %) in an agate mortar. The resulting mixture was heated in an $Al_2O_3$ crucible in air to 650 °C with a heating rate of 5 K $min^{-1}$ with a dwell time of 1.5 h. The product was crushed in an agate mortar and mixed with commercial NMC111 ($LiNi_{0.333}Mn_{0.333}Co_{0.333}O_2$, hereafter as NMC) powder (Sigma Aldrich, >98 %) and a solution of an isomeric mixture of terpineol (Sigma-Aldrich, 99.50 %) with 6 wt% ethyl cellulose (Sigma-Aldrich, 46 cps, 48.00 %) and homogenized in a three-roll mill (50l, Exakt). The resulting ink was printed on sandpaper-polished LLZO separators by screen-printing (E2, Ekra) with a polyester screen (27-120 × 22.5°, Koenen). The wet layers were dried in air for 1 h at 60 °C and finally heated to 750 °C with a heating rate of 5 K $min^{-1}$ and a dwell time of 2 h on a MgO plate with a sheet of LLZO powder. The resulting sintered half-cells were transferred into an Ar glovebox and cleaned with a 1 M citric acid (Sigma-Aldrich, >99.50 %) solution in Tetrahydrofurane (Thermo Scientific, 99.8 %) solution to remove $Li_2CO_3$ impurities.

### 2.3. Cell assembly

First, the anode side of the half-cells were polished with SiC sandpaper to remove possible impurities and obtain a fresh LLZO surface. Then a thin film consisting of a mixture of Li with 3 mol% Na (Li-Na) [52] was pressed on the anode side manually and a Ni-plate was placed on the anode metal. This setup was then heated to 300 °C for 5 min. The resulting full cell was placed in an ECC-Combi (EL-CELL®) cell housing.

### 2.4. Characterization

Top-view scanning electron microscope (SEM) images were taken with a TM3000 SEM (Hitachi), while cross-section images were taken after epoxy embedding and polishing with an EVO 15 (Zeiss), both with a backscattered electron detector and after sputtering a thin Au layer. In addition, energy-dispersive X-ray spectroscopy (EDS) was performed with an EDS detector (Ultim Max 100, Oxford Instruments). The electron acceleration voltage was always set to 15 kV. Density analysis was done with the ImageJ software. Raman spectroscopy mappings (INVIA Qontor, Renishaw) were performed on the top-side and the polished cross-sections with a 532 nm laser (~2.5 mW) and a 2400 l $mm^{-1}$ grating. The spectra were collected with a step size of (x, y) = (1 μm, 1 μm) over an area of 80 × 40 μm with a measuring time of 1 s per spectrum. The spectra were processed, including cosmic ray removal, normalization, and finally averaged to one single spectra. X-ray diffraction (XRD) (D4, Endeavor Bruker) was performed between 10° and 80° in Bragg Brentano geometry. Electrochemical impedance spectroscopy (EIS) and electrochemical cycling tests of the full cells were performed with a potentiostat (VMP-300, Biologic) in a climate chamber (VT 4002EMC, Vötsch Industrietechnik) at 60 °C. For EIS the frequency was varied from 3 MHz to 100 mHz with an electrical field perturbation of 10 mV. The cell was electrochemically cycled between 3.0 V and 4.3 V vs. Li-Na with a constant current of 10 μA, corresponding to a current density of 9.63 μA $cm^{-2}$ and a C-rate of 0.05C. The CAM in the composite cathode is 1.31 mg NMC111, with a specific capacity of NMC111 ~160 mAh $g^{-1}$ [38] the corresponding maximum capacity is 0.21 mAh.

## 3. Results and discussion

The NMC-LBO composite cathodes are processed at 750 °C, which is above the melting point of LBO to mold the NMC particles by LBO. The resulting matrix should consist of an NMC percolation network providing electronic conductivity, while the LBO consists of an ion-conducting percolation network. To prove the successful formation of the composite cathode, top-view, and cross-section SEM images were taken, which are shown in Fig. 2a and b. In the top-view SEM image two different material contrasts and corresponding two different phases are observable. At the top of the surface, there are often particles located, which show straight edges with a bright material contrast. Judging from the contrast alone it could be possible that these particles belong to NMC compared to the darker LBO below, with a much smaller mean atomic number. But generally, agglomerated secondary particles of NMC are spherical [39], as shown in the reference SEM image of the pure NMC in S-Fig. 1. Therefore, it is more probable, that bright particles belong to an undesired secondary phase, which may have formed during the temperature processing of the composite cathode. This fact is even more clearly visible in the cross-section image in Fig. 2b. There the LLZO separator can be seen at the bottom with bright contrast, and the spherical NMC particles in the 10–16 μm thick composite cathode are surrounded by the dark material contrast of LBO. On top of the cathode and in the interface between the composite cathode|separator again many bright particles are observable, which can also be identified as the formed secondary phase mentioned above. The LBO-NMC composite is strongly bounded by the molten LBO, and well-connected. However, the secondary phases are numerous and have a high volumetric ratio of ~25 % and in addition in the top-view images it is possible to see some areas with large cracks up to 13.3 μm in width. Those cracks could maybe form during the melting and densification process, where the material densifies inhomogeneously, resulting in dense regions and cracks in between. Fortunately, those cracks only exist in a vertical direction to the separator, and therefore probably does not have a major impact on

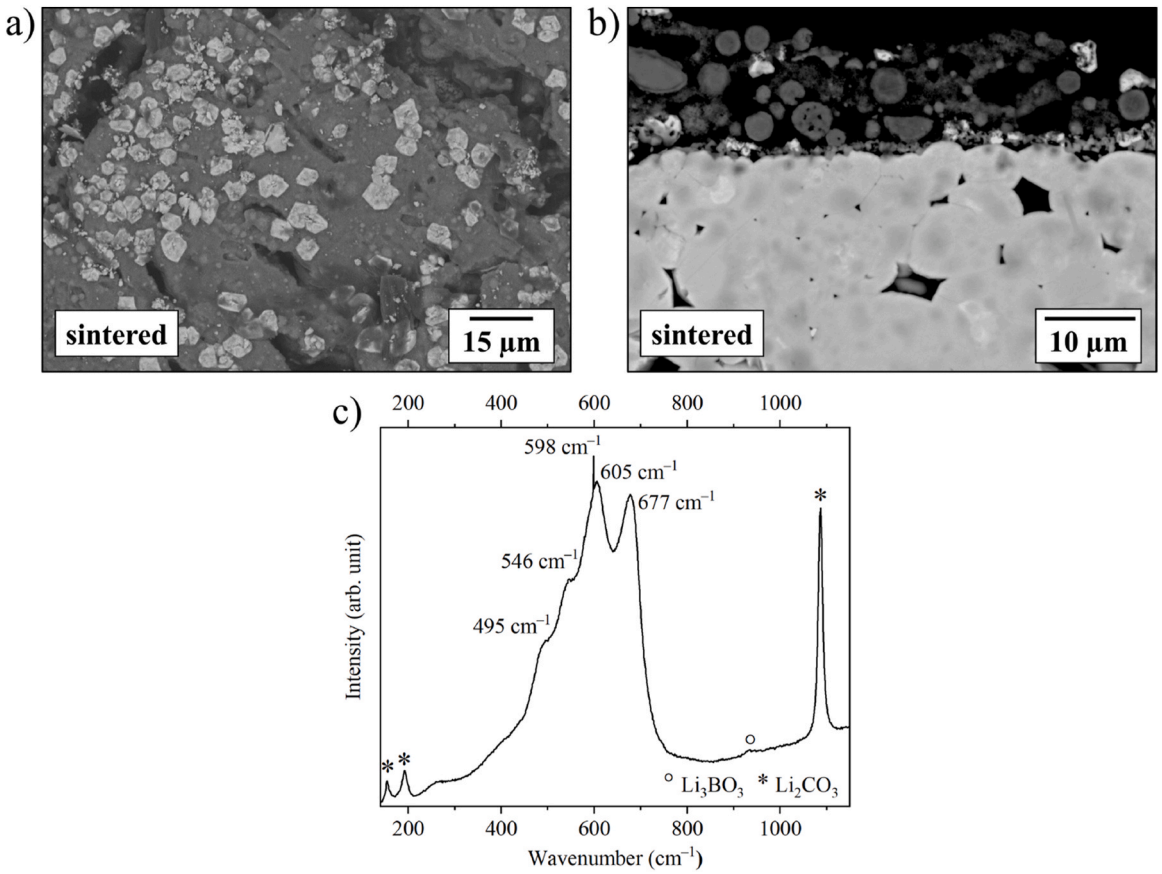


**Fig. 2.** a) top-view, and b) cross-section SEM images of the sintered composite cathode, c) averaged Raman spectra of the cathode.

the ionic and electronic conductivity in the final cell.

To get further information about the phase stability of the battery materials and the formed secondary phases, the sintered cathode was characterized using Raman spectroscopy, shown in Fig. 2c. In the spectrum the typical broad signals of NMC can be observed. The signals at 495, 546, and 605 $cm^{-1}$ belongs to NMC [40–42] and are similar to the Raman reference of the pristine NMC powder, shown in S-Fig. 2. However, there are also some differences observable, like the sharp signal at 598 $cm^{-1}$, which is similar to the Raman signal of $LiCoO_2$, and therefore indicates the presence of a Co-rich secondary phase [43]. At higher wavenumbers, NMC generally shows a shoulder belonging to Mn vibration modes [40–42,44]. In the sintered composite cathode, this shoulder is very pronounced and located at 677 $cm^{-1}$. The combination of those two signals indicates that a certain cation mixing is present in the NMC during sintering. In addition, the catholyte $Li_3BO_3$ is present with a weak signal at 934 $cm^{-1}$ [45] and further, signals at 154, 192, and 1087 $cm^{-1}$ indicating the presence of a $Li_2CO_3$ impurity [46,47]. The XRD analysis also showed the presence of $Li_2CO_3$ and further indicated the formation of a $LaMO_3$ phase with M = Co, Ni, Mn during the high-temperature treatment (S-Fig. 3a).

For further investigation of the composite cathode and its interface to the LLZO separator EDX mappings were performed, which are shown in Fig. 3. The EDX mapping shows the existence of Al-ions in the composite cathode. Since no Al is present in the LBO and NMC, this element is probably diffusing from the LLZO separator, where it is used as substituent of LLZO. This behavior of Al diffusing in NMC from LLZO is already reported for similar structures like $LiCoO_2$, where the presence of Al was also detected in the CAM after co-sintering with LLZO [48]. The Al diffusion can also have a critical influence on the electrolyte interface, e.g. space charge layer formation and requires to be further investigated. Additionally, carbon signals are located in the composite cathode, mainly in the region close to the interface. Since $Li_2CO_3$ was already detected by Raman spectroscopy, the carbonate impurity could be the reason for the C signals. However, it is also possible that the $Li_2CO_3$ reacted with the LBO catholyte to form the even higher-ion-conducting electrolyte $Li_{2.3-x}C_{0.7+x}B_{0.3-x}O_3$ (LCBO), which was already intentionally synthesized by Han et al., by a solid-state reaction of $Li_2CO_3$ and LBO at 650 °C [31]. Another possible origin for the C signals is the epoxy resin which was used for the sample embedding and polishing. The Ni, Mn, and Co mappings show their signals only in the composite cathode and are mainly similar. However, harmonizing with the results of the Raman spectroscopy some disorder in Mn- and Co-cations is observable. One particle for example only shows Mn and Ni signals, while no Co signals are present, and in another particle only Co and Ni and no Mn signals are present. In a Raman mapping of the polished cross-section (S-Fig. 4a) the characteristic Raman signals of $Li_2MnO_3$ were found in some parts of the cathode [49]. The elements of the LLZO Zr, La, and Ta are mainly found in the separator, but Zr and La is also found exactly at the locations where the interface secondary phase in the SEM is located. In addition, the cross-section Raman mapping showed at individual locations of the cathode|separator interface some signals, which correspond to a reaction product of LLZO and CAMs with the composition $Li_{0.5}M_{0.5}La_2O_4$ (M = Co, Ni, Mn) [21,50]. Nevertheless, La and Co can be found in the EDX at different areas overlapping, but also individually not overlapping. Thus, it can be concluded that there must be two different secondary phases at the interface. Although the EDX does not show any significant intensity of Co signals in the LLZO separator, some photoluminescence of Co-doped LLZO (LLZO:Co) can be measured in the separator, like reported in a previous study [21]. This shows that even the reduced processing temperature of 750 °C with the utilization of LBO sintering aid, is high enough to enable cobalt-ion diffusion so that the LLZO:Co phase can be formed in the separator [21].

In order to improve the LLZO|Li interface the residual $Li_2CO_3$ on the LLZO surfaces was removed by exposure to a citric acid solution. The resulting cleaned samples were also investigated by SEM, Raman, XRD, and EDX, as shown in S-Fig. 5and S- Fig. 6. The microstructure and element distribution of the citric acid treated samples do not show any significant difference to those of the sintered samples, but the Raman spectroscopy indicates the successful removal of carbonates indicated by a much lower $Li_2CO_3$ signal intensity. For full cell assembly, a Li-Na anode alloy was attached to the cleaned LLZO half-cell. The Li-Na anode was recently developed by Mann et al. and showed increased performance on the anode side for SSB applications [52]. The

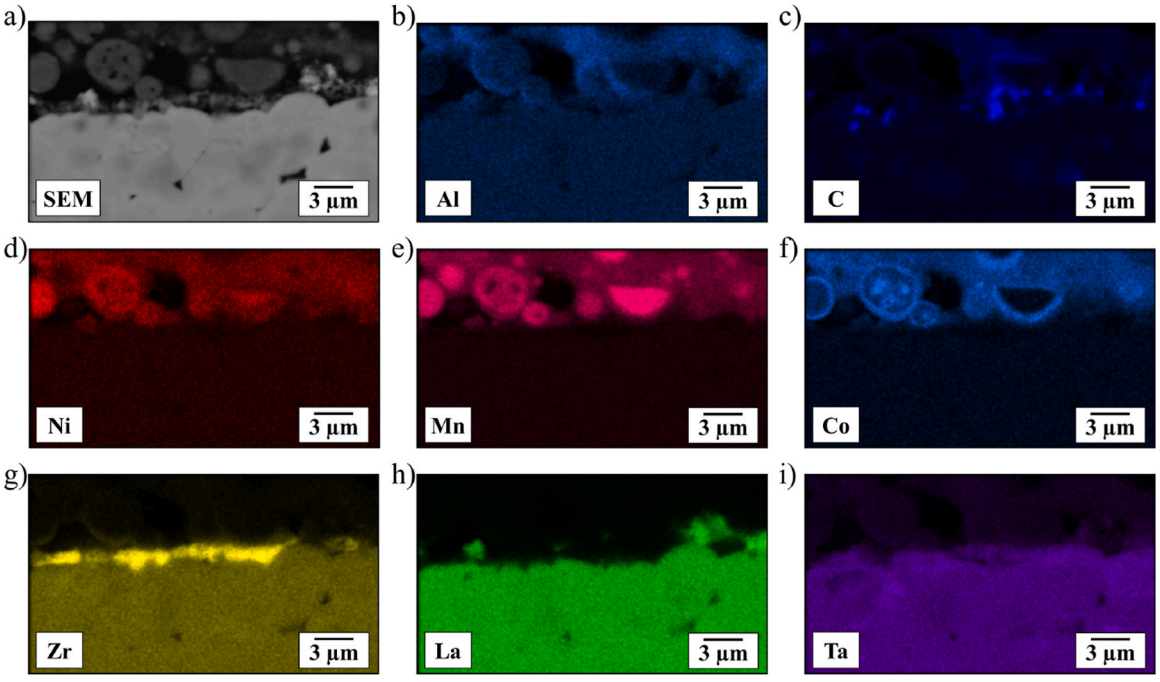


**Fig. 3.** SEM and EDX mappings of the sintered half-cell cross-section: a) SEM image of the investigated area, and EDS mapping of b) Al, c) C, d) Ni, e) Mn, f) Co, g) Zr, h) La, i) Ta.

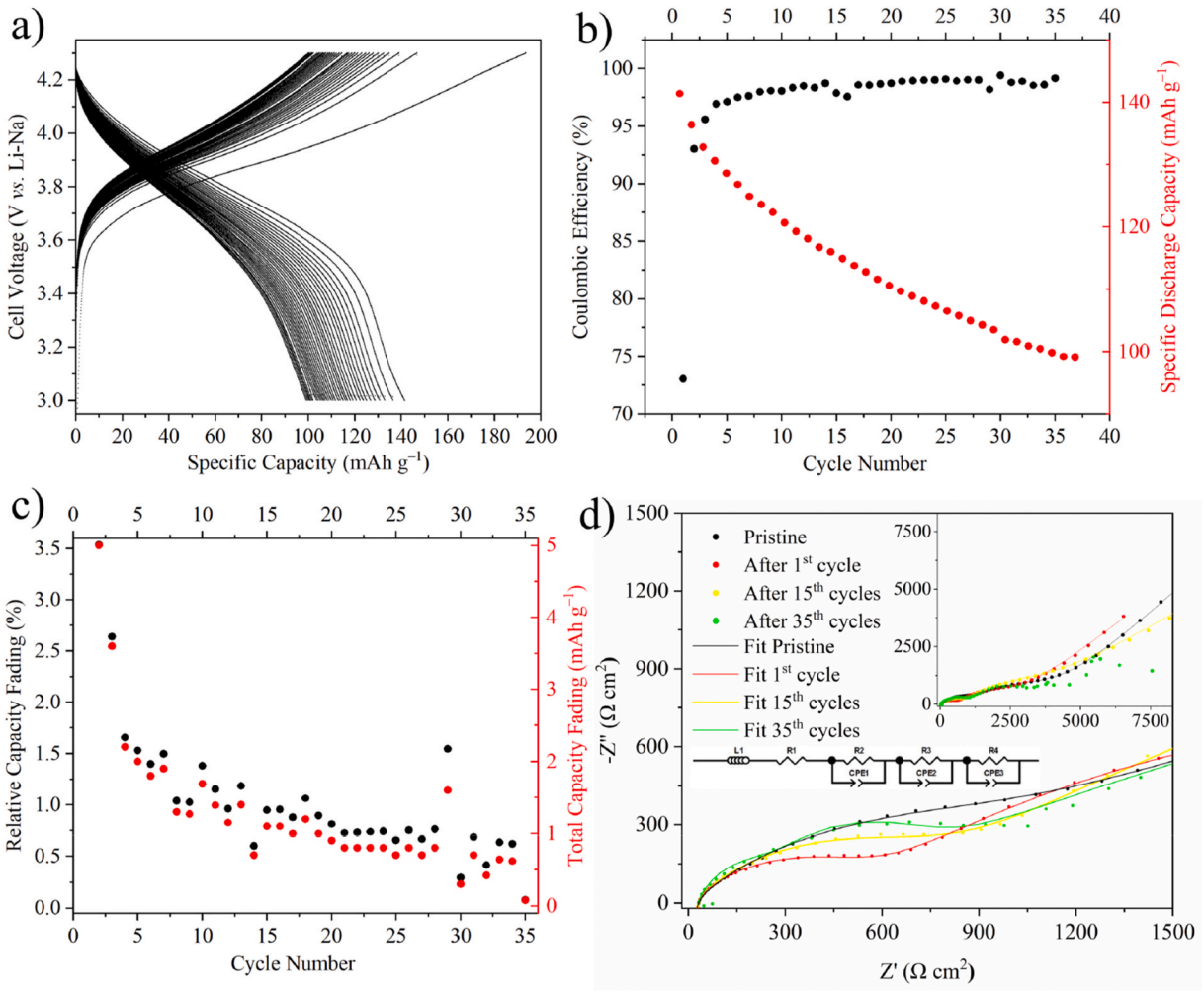


**Fig. 4.** Electrochemical characterization of the assembled full-cell: a) GCPL data of 34 cycles with b) the corresponding Coulombic efficiency and discharge capacity, and c) relative and total capacity fade, d) EIS after different cycles, with the fitted data and the used equivalent circuit.

galvanostatic cycling with potential limitation (GCPL) of this cell (Fig. 4a) proofs the electrochemical activity of the LBO-NMC composite cathode. An initial discharge capacity of 140 mAh g$^{-1}$ was obtained, which corresponds to a capacity utilization of around 88 %, when considering 160 mAh g$^{-1}$ as practical capacity of NMC111. The first charging process indicates a formation process by a high irreversible capacity. Corresponding to that the coulombic efficiency is low at the beginning and is increasing to almost 99 % in the following cycles (Fig. 4b). However, the discharge capacity fades over the subsequent cycles (Fig. 4c). The strongest capacity fading is observable in the first charge with ~3.5 % or ~5 mAh g$^{-1}$ per cycle, and then the fading ratio reduces until a fading of only ~0.8 % or ~0.08 mAh g$^{-1}$ per cycle is reached in the 34th cycle. Nevertheless, the capacity retention is 99.2 mAh g$^{-1}$ after 34 cycles corresponding to a CAM utilization of 62 % (that means 26 % of the initial cathode capacity is lost) [38]. Compared to other SSB with similar cell designs (electrolyte: LLZO, LBO; CAM: LCO, NMC) the here reported cell design with the LBO catholyte shows a significant smaller capacity fading during cycling compared to literature, like shown in Table 1 [8–11,26]. The SSB of Han et al. [31] with the LCO + LLZO + LCBO/LLZO/Li cell design, which is very similar to the cell presented in this work, but still contains LLZO particles in the composite cathode, has a very similar capacity fading compared to our pure LBO catholyte cells. However, an even better performance without any LBO was achieved by Hou et al. [24], who demonstrated a cell with only 13.3 % capacity fading after 30 cycles.

Those values show that the LBO catholyte can have a positive impact on the cycling stability of LLZO-based cells, by reducing the capacity fade per cycle. By preventing the contact between the CAM and LLZO, the general electrochemical cycling instability of those materials [23] is bypassed and the cell shows more stable cycling. However, the results of Hou et al. [24] also show that besides cell chemistry also the material synthesis and cell fabrication have a crucial impact. Nevertheless, it could be that an optimized cell chemistry with the use of catholytes could further enhance already good-performing SSBs like those of Hou et al. In addition, some properties like particle size, particle size ratio of

**Table 1**
Comparison of the capacity fading of different LLZO-based SSBs. The cell chemistry of this work is: NMC111 + LBO / LLZO / Li-Na.

| Ref. | Cell chemistry[a] | Cycle | Capacity fading[b] | |
|---|---|---|---|---|
| | | | Ref. | This work |
| [11] | LCO + LLZO / LLZO / Li-In | 5th | 35.5 % | 9.1 % |
| [9] | LCO + LLZO / LLZO / Li-In | 6th | 36.6 % | 10.3 % |
| [8] | LCO + LLZO / LLZO / Li-In | 10th | 72.5 % | 14.7 % |
| [26] | NMC811 + LLZO + LBO / LLZO / Li | 30th | 41.3 % | 28.7 % |
| [10] | LCO + LLZO / LLZO / Li-In | 30th | 44.3 % | 28.7 % |
| [31] | LCO + LLZO + LCBO / LLZO / Li | 30th | 29.2 % | 28.7 % |
| [24] | LCO + LLZO / LLZO / Li | 30th | 13.3 % | 28.7 % |

[a] Cell chemistry given as: Cathode/Separator/Anode.
[b] The capacity fading is given in % from the 1st cycle to the corresponding cycle number of the corresponding table column.

NMC to LBO, and the LBO composition (LBO to LCBO), could further influence the cycling stability.

Going a hand with the capacity fading the cell resistance is increasing during electrochemical cycling (Fig. 4d). First, the total resistance of the cell reduces after the 1st cycle, but then in the subsequent cycles, the resistance increases with increasing cycle number. The spectrum was fitted using an equivalent circuit as shown (Fig. 4d). The *R*-CPE elements represent the impedance of the grain boundaries and the interfacial impedances of both electrode layers. The semicircle corresponding to the bulk resistance cannot be resolved at this temperature, therefore it is approximated with good accuracy by a resistance *R*. It is shown that the resistance decreases from the uncycled pristine state with a total impedance of 4185 Ω to the first cycle with 2827 Ω, probably due to formation processes. However, then the resistance constantly increases to 3274 Ω after 15 cycles and 6671 Ω after 35 cycles.

To get a better understanding about the electrochemical degradation process, the microstructure and phase analysis of the cycled sample was performed, which is shown in Fig. 5. By the comparison of the SEM images of the sintered and cycled sample surface (Fig. 5a), cracks in the cycled LBO can be observed, which indicates a mechanical instability of the composite cathode during electrochemical cycling. Those cracks could occur due to the general volume change of the CAM during lithiation and delithiation [51], but it could also occur due to the formation of a secondary phase, which also hypothetical could go along with a volume expansion. When the resulting stress of such volume expansions is released, the observed cracking of the LBO catholyte can be the result. Further, by observing the cross-sectional SEM images of the cycled sample an even worse phenomena can be observed, where the composite cathode delaminates from the LLZO separator. The delamination could be a result of the electrochemical cycling, but also cell disassembly and the SEM sample preparation process could lead to a delamination. However, since the top-view SEM images of a cell after the first cycle (S-Fig. 7) already show an increased number of cracks, a contact loss between NMC and LBO particles as well as between composite cathode and LLZO separator are probably the reasons for the degradation.

Those results clearly illustrate that despite the positive effect of LBO with reduced capacity fading in electrochemical cycling, as shown in Table 1, the overall long-term cycling stability of LBO is not given. The cycling induced cracking of the LBO will finally lead to a failure of the cathode since the cracks sum up and reduce particle bonding and causes mechanical instability of the whole composite cathode layer. Overall, this study demonstrates that capacity fading can be mitigated by modifying the composition of the composite cathode, but this is still accompanied by electrochemically induced mechanical degradation.

Further, the Raman spectra of the cycled composite cathode (Fig. 5c) has similar NMC signals like the fresh composite cathode, but the cycled sample show no signals of Ni-O vibrations in the low wavenumber region, while the prominent shoulder of the Mn-O vibrations is still present at 668 $cm^{-1}$. Therefore, it is possible that a change in the NMC structure during the electrochemical cycling occurred. However, due to the high noise in the measurement no other secondary phases were observed. In addition, the XRD data after one and 34 cycles also shows the same phases of LLZO, NMC, LBO, and the only observed secondary phases are still $LaMO_3$ and $Li_2CO_3$, like in the cathode before cycling (S-Fig. 3b and c).

The secondary phases $LaMO_3$ (M = Co, Ni, Mn) and $Li_{0.5}M_{0.5}La_2O_4$ (M = Co, Ni, Mn) are known side phases for this kind of material system [50], which alone did not affect the capacity fading in a positive way [50]. However, it cannot be ruled out that the side phases $LaMO_3$ (M = Co, Ni, Mn) and $Li_{0.5}M_{0.5}La_2O_4$ (M = Co, Ni, Mn) could have synergistic effects with the $Li_3BO_3$. For or against this theory is no evidence given in this work and further experiments, above the scope of this work, has to be done to completely reveal the influence of the side phases to the system.

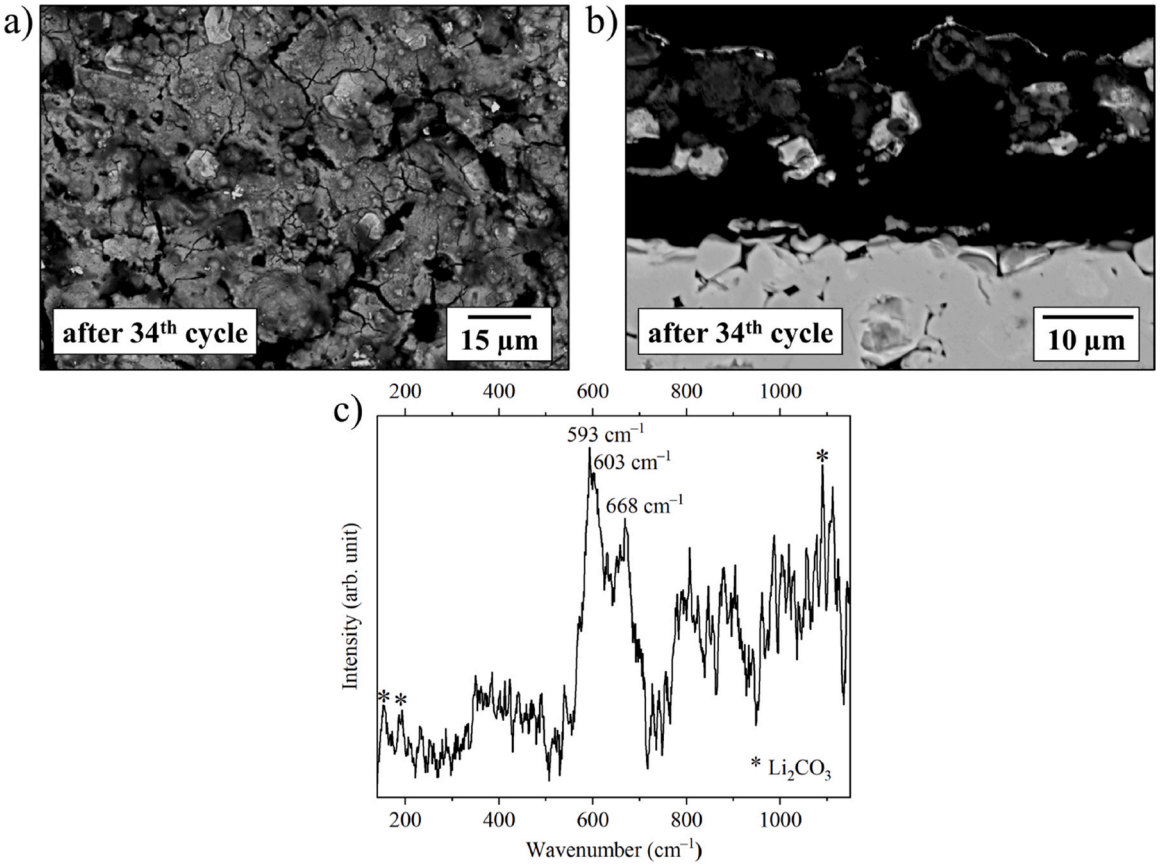


**Fig. 5.** a) top-view, and b) cross-section SEM images of the composite cathode after the 34th electrochemical cycles, and c) averaged Raman spectra of the cathode.

The EDX measurements of the fully cycled cross-section (S-Fig. 9) does not show electrochemically induced changes, when comparing with the results of the sintered sample (Fig. 3) and the sample after the first cycle (S-Fig. 8). Nevertheless, electrochemical changes cannot be ruled out, but must be tested using high-resolution techniques.

## 4. Conclusion

In this study, SSBs with a Li-Na anode, an LLZO separator and a NMC111-LBO composite cathode were fabricated at 750 °C. The sintering of the NMC111-LBO based composite cathodes resulted in well-connected layers with $LaMO_3$ (M = Co, Ni, Mn) and $Li_{0.5}M_{0.5}La_2O_4$ (M = Co, Ni, Mn) as secondary phases. The cells showed electrochemically activity over 34 cycles with a reduced capacity fading during cycling, compared to other LLZO-based SSB, with and without LBO in the composite cathode. However, microstructural investigations showed that the LBO catholyte forms severe cracks during cycling, which probalby leads to the observed capacity fading of the NMC111-LBOcells. It was shown that the changed cell composition can improve the cycling behavior, but other materials then LBO, which mitigate the stresses during cycling and thus improve the mechanical stability, must be found.

## CRediT authorship contribution statement

**Walter Sebastian Scheld:** Writing – review & editing, Writing – original draft, Visualization, Validation, Project administration, Methodology, Investigation, Data curation, Conceptualization. **Yannic Collette:** Methodology, Investigation, Data curation. **Kaouther Touidjine:** Methodology, Investigation, Data curation. **Christoph Roitzheim:** Writing – review & editing, Validation, Data curation. **Yoo Jung Sohn:** Writing – review & editing, Validation, Data curation. **Dina Fattakhova-Rohlfing:** Writing – review & editing, Funding acquisition.

## Declaration of competing interest

The authors declare that they have no known competing financial interests or personal relationships that could have appeared to influence the work reported in this paper.

## Acknowledgment

This work was funded by the German Federal Ministry of Education and Research (BMBF) as part of the FB2-Oxid (grant no. 13XP0434A) and CatSE$^2$ (grant no. 13XP0510A) projects. This work was partly funded by the European Union's Horizon2020 Research and Innovation Program under the Marie Skłodowska-Curie Action PhD COFUND (grant no. 945357).

## Appendix A. Supplementary data

Supplementary data to this article can be found online at https://doi.org/10.1016/j.jpowsour.2025.237322.

## Data availability

Data will be made available on request.

## References

[1] J. Janek, W.G. Zeier, Nat. Energy 1 (2016).
[2] Y. Xiao, Y. Wang, S.-H. Bo, J.C. Kim, L.J. Miara, G. Ceder, Nat. Rev. Mater. 5 (2019) 105–126.
[3] N. Zhao, W. Khokhar, Z. Bi, C. Shi, X. Guo, L.-Z. Fan, C.-W. Nan, Joule 3 (2019) 1190–1199.
[4] C. Wang, K. Fu, S.P. Kammampata, D.W. McOwen, A.J. Samson, L. Zhang, G. T. Hitz, A.M. Nolan, E.D. Wachsman, Y. Mo, V. Thangadurai, L. Hu, Chem. Rev. 120 (2020) 4257–4300.
[5] T. Thompson, S. Yu, L. Williams, R.D. Schmidt, R. Garcia-Mendez, J. Wolfenstine, J.L. Allen, E. Kioupakis, D.J. Siegel, J. Sakamoto, ACS Energy Lett. 2 (2017) 462–468.
[6] R. Murugan, V. Thangadurai, W. Weppner, Angew. Chem. Int. Ed. 46 (2007) 7778–7781.
[7] R. Ye, N. Hamzelui, M. Ihrig, M. Finsterbusch, E. Figgemeier, ACS Sustain. Chem. Eng. 10 (2022) 7613–7624.
[8] W.S. Scheld, J.N. Ebert, M. Scherer, L. Fulanovic, L. Porz, C. Dellen, M. Ihrig, S. Uhlenbruck, M. Finsterbusch, O. Guillon, D. Fattakhova-Rohlfing, W. Rheinheimer, J. Eur. Ceram. Soc. 44 (2024) 3039–3048.
[9] W.S. Scheld, S. Lobe, C. Dellen, M. Ihrig, G. Hauschen, L.C. Hoff, M. Finsterbusch, S. Uhlenbruck, O. Guillon, D. Fattakhova-Rohlfing, J. Power Sources 545 (2022) 231872.
[10] C.-L. Tsai, Q. Ma, C. Dellen, S. Lobe, F. Vondahlen, A. Windmüller, D. Grüner, H. Zheng, S. Uhlenbruck, M. Finsterbusch, F. Tietz, D. Fattakhova-Rohlfing, H. P. Buchkremer, O. Guillon, Sustain. Energy Fuels 3 (2019) 280–291.
[11] M. Ihrig, M. Finsterbusch, C.-L. Tsai, A.M. Laptev, C.-h. Tu, M. Bram, Y.J. Sohn, R. Ye, S. Sevinc, S.-k. Lin, D. Fattakhova-Rohlfing, O. Guillon, J. Power Sources 482 (2021) 228905.
[12] M. Finsterbusch, T. Danner, C.L. Tsai, S. Uhlenbruck, A. Latz, O. Guillon, ACS Appl. Mater. Interfaces 10 (2018) 22329–22339.
[13] K.J. Kim, J.L.M. Rupp, Energy Environ. Sci. 13 (2020) 4930–4945.
[14] M. Rosen, M. Finsterbusch, O. Guillon, D. Fattakhova-Rohlfing, J. Mater. Chem. A 10 (2022) 2320–2326.
[15] S. Uhlenbruck, J. Dornseiffer, S. Lobe, C. Dellen, C.-L. Tsai, B. Gotzen, D. Sebold, M. Finsterbusch, O. Guillon, J. Electroceram. 38 (2016) 197–206.
[16] J. Wakasugi, H. Munakata, K. Kanamura, J. Electrochem. Soc. Jpn. 85 (2017) 77–81.
[17] N. Zhang, X. Long, Z. Wang, P. Yu, F. Han, J. Fu, G. Ren, Y. Wu, S. Zheng, W. Huang, C. Wang, H. Li, X. Liu, ACS Appl. Energy Mater. 1 (2018) 5968–5976.
[18] Y. Ren, T. Liu, Y. Shen, Y. Lin, C.-W. Nan, J. Materiomics 2 (2016) 256–264.
[19] L.J. Miara, W.D. Richards, Y.E. Wang, G. Ceder, Chem. Mater. 27 (2015) 4040–4047.
[20] L. Miara, A. Windmuller, C.L. Tsai, W.D. Richards, Q. Ma, S. Uhlenbruck, O. Guillon, G. Ceder, ACS Appl. Mater. Interfaces 8 (2016) 26842–26850.
[21] W.S. Scheld, K. Kim, C. Schwab, A.C. Moy, S.K. Jiang, M. Mann, C. Dellen, Y. J. Sohn, S. Lobe, M. Ihrig, M.G. Danner, C.Y. Chang, S. Uhlenbruck, E. D. Wachsman, B.J. Hwang, J. Sakamoto, L.F. Wan, B.C. Wood, M. Finsterbusch, D. Fattakhova-Rohlfing, Adv. Funct. Mater. 33 (2023) 2302939.
[22] M.M.U. Din, L. Ladenstein, J. Ring, D. Knez, S. Smetaczek, M. Kubicek, M. Sadeqi-Moqadam, S. Ganschow, E. Salagre, E.G. Michel, S. Lode, G. Kothleitner, I. Dugulan, J.G. Smith, A. Limbeck, J. Fleig, D.J. Siegel, G.J. Redhammer, D. Rettenwander, Adv. Funct. Mater. 33 (2023).
[23] M. Ihrig, M. Finsterbusch, A.M. Laptev, C.H. Tu, N.T.T. Tran, C.A. Lin, L.Y. Kuo, R. Ye, Y.J. Sohn, P. Kaghazchi, S.K. Lin, D. Fattakhova-Rohlfing, O. Guillon, ACS Appl. Mater. Interfaces 14 (2022) 11288–11299.
[24] A.Y. Hou, C.Y. Huang, C.L. Tsai, C.W. Huang, R. Schierholz, H.Y. Lo, H. Tempel, H. Kungl, R.A. Eichel, J.K. Chang, W.W. Wu, Adv. Sci. 10 (2023) e2205012.
[25] S. Ohta, S. Komagata, J. Seki, T. Saeki, S. Morishita, T. Asaoka, J. Power Sources 238 (2013) 53–56.
[26] C. Roitzheim, Y.J. Sohn, L.-Y. Kuo, G. Häuschen, M. Mann, D. Sebold, M. Finsterbusch, P. Kaghazchi, O. Guillon, D. Fattakhova-Rohlfing, ACS Appl. Energy Mater. 5 (2022) 6913–6926.
[27] H. Xie, C. Li, W.H. Kan, M. Avdeev, C. Zhu, Z. Zhao, X. Chu, D. Mu, F. Wu, J. Mater. Chem. A 7 (2019) 20633–20639.
[28] R.A. Jonson, P.J. McGinn, Solid State Ionics 323 (2018) 49–55.
[29] Z. Tang, J. Choi, J.L. Lorie Lopez, A.C. Co, C.J. Brooks, J.R. Sayre, J.-H. Kim, ACS Appl. Energy Mater. 5 (2022) 12132–12142.
[30] K. Park, B.-C. Yu, J.-W. Jung, Y. Li, W. Zhou, H. Gao, S. Son, J.B. Goodenough, Chem. Mater. 28 (2016) 8051–8059.
[31] F. Han, J. Yue, C. Chen, N. Zhao, X. Fan, Z. Ma, T. Gao, F. Wang, X. Guo, C. Wang, Joule 2 (2018) 497–508.
[32] Y. Zhang, Z. Tang, Y. Mei, Y. Xiao, X. Xiang, D. Luo, J. Deng, Appl. Surf. Sci. 630 (2023).
[33] N.C. Rosero-Navarro, T. Yamashita, A. Miura, M. Higuchi, K. Tadanaga, Solid State Ionics 285 (2016) 6–12.
[34] C.-L. Tsai, E. Dashjav, E.-M. Hammer, M. Finsterbusch, F. Tietz, S. Uhlenbruck, H. P. Buchkremer, J. Electroceram. 35 (2015) 25–32.
[35] M. Mann, M. Kupers, G. Hauschen, M. Finsterbusch, D. Fattakhova-Rohlfing, O. Guillon, Materials (2021) 14.
[36] M. Mann, M. Küpers, G. Häuschen, M. Finsterbusch, D. Fattakhova-Rohlfing, O. Guillon, Ionics 28 (2021) 53–62.
[37] C. Schwab, G. Häuschen, M. Mann, C. Roitzheim, O. Guillon, D. Fattakhova-Rohlfing, M. Finsterbusch, J. Mater. Chem. A 11 (2023) 5670–5680.
[38] A.M. Hashem, A.E. Abdel-Ghany, H.M. Abuzeid, H. Ehrenberg, A. Mauger, H. Groult, C.M. Julien, ECS Trans. 50 (2013) 91–96.
[39] R. Xu, L.S. de Vasconcelos, J. Shi, J. Li, K. Zhao, Exp. Mech. 58 (2017) 549–559.
[40] Q. Wu, V.A. Maroni, D.J. Gosztola, D.J. Miller, D.W. Dees, W. Lu, J. Electrochem. Soc. 162 (2015) A1255–A1264.
[41] X. Zhang, A. Mauger, Q. Lu, H. Groult, L. Perrigaud, F. Gendron, C.M. Julien, Electrochim. Acta 55 (2010) 6440–6449.
[42] A.M. Hashem, A.E. Abdel-Ghany, M. Scheuermann, S. Indris, H. Ehrenberg, A. Mauger, C.M. Julien, Materials (2019) 12.

[43] T. Gross, C. Hess, J. Power Sources 256 (2014) 220–225.
[44] C. Ghanty, B. Markovsky, E.M. Erickson, M. Talianker, O. Haik, Y. Tal-Yossef, A. Mor, D. Aurbach, J. Lampert, A. Volkov, J.Y. Shin, A. Garsuch, F.F. Chesneau, C. Erk, Chemelectrochem 2 (2015) 1479–1486.
[45] M. Tatsumisago, R. Takano, M. Nose, K. Nagao, A. Kato, A. Sakuda, K. Tadanaga, A. Hayashi, J. Ceram. Soc. Japan 125 (2017) 433–437.
[46] D. Peltzer, J. Múnera, L. Cornaglia, RSC Adv. 6 (2016) 8222–8231.
[47] R. Ye, M. Ihrig, N. Imanishi, M. Finsterbusch, E. Figgemeier, ChemSusChem 14 (2021) 4397–4407.
[48] M. Ihrig, L.Y. Kuo, S. Lobe, A.M. Laptev, C.A. Lin, C.H. Tu, R. Ye, P. Kaghazchi, L. Cressa, S. Eswara, S.K. Lin, O. Guillon, D. Fattakhova-Rohlfing, M. Finsterbusch, ACS Appl. Mater. Interfaces 15 (2023) 4101–4112.
[49] F.A. Susai, M. Talianker, J. Liu, Rosy, T. Paul, Y. Grinblat, E. Erickson, M. Noked, L. Burstein, A.I. Frenkel, Y. Tsur, B. Markovsky, D. Aurbach, Materials (2020) 13.
[50] A. Bauer, C. Roitzheim, S. Lobe, Y.J. Sohn, D. Sebold, W.S. Scheld, M. Finsterbusch, O. Guillon, D. Fattakhova-Rohlfing, S. Uhlenbruck, Chem. Mater. 35 (2023) 8958–8968.
[51] R. Koerver, W. Zhang, L. de Biasi, S. Schweidler, A.O. Kondrakov, S. Kolling, T. Brezesinski, P. Hartmann, W.G. Zeier, J. Janek, Energy Environ. Sci. 11 (2018) 2142–2158.
[52] M. Mann, C. Schwab, L.C.P. dos Santos, R. Spatschek, D. Fattakhova-Rohlfing, M. Finsterbusch, Energy Storage Mater. 74 (2025) 103975.